Research on Fractal Model of Load Distribution and Axial Stiffness of Planetary Roller Screw Mechanism Considering Surface Roughness and Friction Factor

Xing Du,* Bingkui Chen, Rongrong Liu, and Chaoyang Li

The effects of surface roughness and material properties of the planetary roller screw mechanism (PRSM) on the axial stiffness and load distribution are rarely studied. In this paper, the load distribution model is presented by incorporating into friction factor and surface microtopography. The microcontact model is built by considering elastic and plastic regimes to calculate the total actual contact area. Moreover, the load distribution model is modified by introducing surface microcontact coefficient. Then, the influences of the nut position, fractal dimension, fractal roughness, friction factor, axial load, and material yield strength on the axial stiffness and load distribution are studied in detail. The numerical results show that the axial stiffness rises with the increment of the nut position, axial load, fractal dimension, and yield strength, and reduces with the fractal roughness and friction factor increasing. In addition, the uniformity of the load distribution increases with the increment of the fractal roughness, and drops with the increase of the fractal dimension and material yield strength. This investigation lays the foundation for the design, manufacturing, and use of the PRSM.

1. Introduction

The planetary roller screw mechanism (PRSM), as a key linear transmission component of electromechanical system, has been widely used in aircrafts,[1,2] weaponry, telecommunication satellites, robots, and petrochemical industries because of its advantages such as high precision, high load ratio, high reliability, and high stability. These characteristics are affected by contact stiffness and contact load distribution. In fact, the differences, derived from machining methods, manufacturing accuracies, heat treatment methods, and surface wear, play an important role in the axial stiffness and load distribution. These differences result in the variations of the surface topography and material properties, while the effects of these on the axial stiffness and load distribution have been almost ignored in the past.

X. Du
School of Mechatronics Engineering
Nanchang University
Nanchang 330031, P. R. China
E-mail: duxing@ncu.edu.cn
B. Chen, R. Liu, C. Li
State Key Laboratory of Mechanical Transmissions
Chongqing University
Chongqing 400044, P. R. China

The ORCID identification number(s) for the author(s) of this article can be found under https://doi.org/10.1002/adts.202100399

A large number of studies on the axial stiffness and load distribution have been carried out in the past 20 years. For load distribution analysis, Zhang et al.[3,4] proposed an efficient model to compute load distribution over threads of the PRSM considering the effect of the pitch deviation, and presented an effective method that the roller threads were redesigned. The results showed it was beneficial to achieve even load distribution to a certain extent. Du et al.[5] proposed the modeling approach of the load distribution by incorporating the axial load, radial load, and machining error, and revealed that the contact force periodically changed as the increase of the thread number as the PRSM was subjected to the radial load. For axial stiffness analysis, Jones and Velinsky[6] presented a stiffness model by the direct stiffness method and estimated the contact forces over threads and the overall stiffness of the PRSM. Abevi et al.[7] proposed a numerical model of the inverted PRSM (IPRSM) to estimate the axial stiffness and load distribution. The results revealed that the load distributions over threads were uneven and the static behavior of the IPRSM was affected by the configurations. Abevi et al.[8] proposed a nonlinear contact model by using the equivalent bar, beam, and nonlinear spring in order to compute the contact forces over threads and axial stiffness. The results revealed that the load types were vital to the load distribution. Ma et al.[9] proposed an analytical model of the axial stiffness by considering the Hertz contact deformation, screw shaft deformation, and thread deformation, and an accuracy coefficient was incorporated into the model. The results revealed that the axial load and nut position played a significant role on the axial stiffness.

The above investigations have paved the foundation for static analysis of the load distribution and axial stiffness, but the surface roughness and material property are not considered. The surface morphology and material property had an important influence on the contact stiffness and contact force, which were investigated in the spherical pump,[10] mechanical joint,[11] and spur gear.[12] In these works, the fractal theory was applied in computing the contact load and contact stiffness, because the rough surface morphology was characterized by the fractal functions. These functions were continuity,[13] nondifferentiability,[14] and self-affinity[15] so that it can be very close to the actual microtopography of the thread surface. However, the relation among the

contact stiffness, contact load, and surface morphology are difficult to be established. Zhao et al.[12] proposed an improved model of the spur gear by considering the effect of the surface roughness in order to compute time-varying mesh stiffness and load sharing ratio. The results revealed that the meshing characteristics were affected by the surface roughness and friction coefficient. Chang et al.[16] presented an improved mathematical model to calculate the contact stiffness of the joint interface based on the fractal theory and revealed that the dynamic characteristics of a machine tool structure was notably influenced by the contact stiffness.

The actual contact area and contact force are closely related to the contact stiffness and load distribution. Hence, it is vital to estimate the above contact parameters based on the multiscale contact mechanics. The previous multiscale contact mechanic models[17,18] mainly concentrated on two rough surfaces. However, the thread profiles of the PRSM mainly includes straight and circular types. In other words, the main contact modes between the profiles of two meshing surfaces could be straight–straight, straight–convex, and convex–concave in engineering application. As a result, the previous models are not suitable for the straight–convex contact. Therefore, it is necessary to introduce the surface microcontact efficient in order to modify the multiscale contact mechanical model.

This paper targets at presenting an efficient approach to estimate the load distribution and axial stiffness by incorporating surface roughness, material properties, and operating conditions. The main framework of this study is as follows: in Section 2, the axial stiffness and load distribution models suitable for the PRSM are presented by incorporating into the friction factor and surface microtopography. The rough surface topography is characterized by the 2D Majumdar–Bhushan (MB) function. The multiscale fractal contact model is built by considering elastic and plastic contact regimes. Moreover, the model is modified by introducing the surface microcontact coefficient in order to accurately characterize the contact characteristics of the thread profile. In Section 3, the numerical examples are carried out, and the model correctness is validated by comparing with the previous results. Moreover, the influences of the nut position, fractal dimension, fractal roughness, friction factor, and yield strength on the axial stiffness and load distribution are investigated in detail. In Section 4, the conclusions are drawn based on the previous analysis.

2. Mathematical Model

The structure of the PRSM is shown in **Figure 1**. The basic principle is that the screw rotates, driving the roller to revolve around the screw shaft axis while rotating on its own axis, and then the roller drives the nut to move in the axial direction.

2.1. Axial Stiffness

The axial stiffness of the PRSM is directly related to the axial load and axial deformation, which is defined by

$$K_a = \frac{\Delta F_a}{\Delta \delta_a} \tag{1}$$

where $\Delta \delta_a$ is the axial deformation, and the deformations mainly include the screw shaft deformation δ_S, thread deformation δ_T,
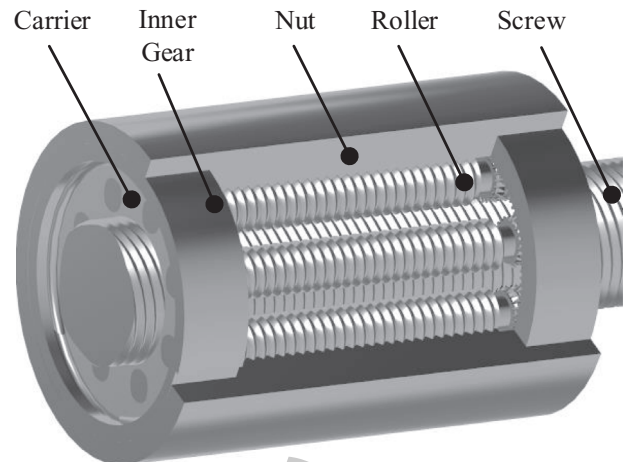

Figure 1. Planetary roller screw mechanism.

and contact deformation δ_C.[9] According to ref. [9], the axial stiffness considering the accuracy coefficient is defined by

$$K_a = \frac{F_a}{\delta_S + \chi(\delta_T + \delta_C)} \tag{2}$$

where χ is the accuracy coefficient and $\chi = 1.818$. F_a is the total axial load.

2.2. Screw Shaft Deformation

The screw shaft deformation mainly includes the tension or pressure deformation, and torsional deformation, as shown in **Figure 2**. Then the deformation can be written by[19]

$$\delta_S = \frac{F_a L_N}{\pi E r_S^2} + \frac{2 F_a L_N P_S^2}{\pi^3 r_S^4 \eta S_G} \tag{3}$$

where L_N denotes the nut position, E is Young's elastic modulus of the material, r_S is the nominal radius of the screw, P_S is the lead of the screw, η is the working efficiency of the PRSM, and S_G is the shear modulus.

2.3. Thread Deformation and Stiffness

The axial thread deformation of the PRSM mainly includes the deformations caused by the bending force, shear force, thread root lean, thread root shear, and radial shrinkage or radial expansion, as shown in **Figure 3**. These deformations are calculated in detail as follows[20]

1) Deformation caused by bending force

$$\delta_{T1} = (1 - v^2) \frac{3 F_{ri} \cos \beta \cos \lambda}{4E} \left\{ \left[1 - \left(2 - \frac{c_t}{a_t} \right)^2 \right. \right.$$
$$\left. \left. + 2 \ln \left(\frac{a_t}{c_t} \right) \right] \cot^3 \beta - 4 \left(\frac{h_f}{a_t} \right) \tan \beta \right\} \tag{4}$$

ADVANCED
SCIENCE NEWS
www.advancedsciencenews.com

ADVANCED
THEORY AND
SIMULATIONS
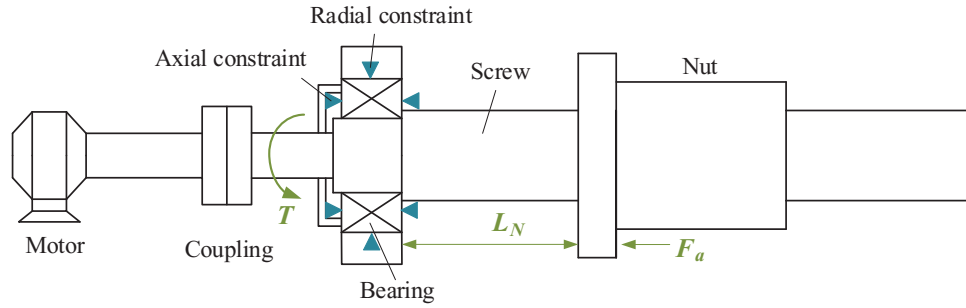www.advtheorysimul.com

Figure 2. Contact diagram of the contact point of the PRSM.
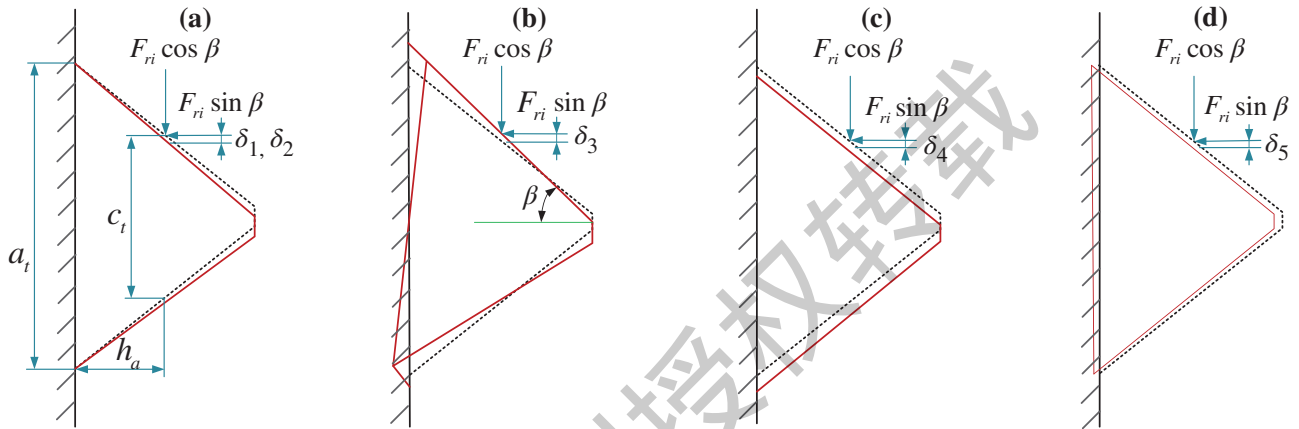

Figure 3. Thread deformations of the PRSM caused by various reasons: a) deformation δ_1 caused by bending force or deformation δ_2 caused by shear force; b) deformation δ_3 caused by thread root lean; c) deformation δ_5 caused by thread root shear; d) deformation δ_6 caused by radial shrinkage.

where ν is the poisson ratio. F_{ri} is normal contact force at ith contact point. β and λ are the flank angle and helix angle, respectively. a_t and c_t are the thickness of the thread root and thread thickness, respectively. h_f is the thread root height.

2) Deformation caused by shear force

$$\delta_{T2} = (1+\nu)\frac{6F_{ri}\cos\beta\cos\lambda}{5E}\cot\beta\ln\left(\frac{a_t}{c_t}\right) \quad (5)$$

3) Deformation caused by thread root lean

$$\delta_{T3i} = (1-\nu^2)\frac{12F_{ri}\cos\beta\cos\lambda h_f}{\pi E a_t^2}\left(h_f - \frac{c_t\tan\beta}{2}\right) \quad (6)$$

4) Deformation caused by thread root shear

$$\delta_{T4} = (1-\nu^2)\frac{2F_{ri}\cos\beta\cos\lambda}{\pi E}\left[\frac{p}{a_t}\ln\left(\frac{p+0.5a_t}{p-0.5a_t}\right)\right.$$
$$\left. + 0.5\ln\left(\frac{4p^2-a_t^2}{a_t^2}\right)\right] \quad (7)$$

where, p is the pitch.

5) Deformation caused by radial shrinkage or radial expansion

$$\delta_{T5n} = \left(\frac{D_0^2+d_p^2}{D_0^2-d_p^2}+\nu\right)\frac{F_{ri}d_p\sin\beta\tan\beta}{2pE}, \quad (\text{nut}) \quad (8)$$

$$\delta_{T5e} = (1-\nu)\frac{F_{ri}d_p\sin\beta\tan\beta}{2pE}, \text{(screw or roller)} \quad (9)$$

where, D_0 and d_p are the external diameter of the nut and thread effective diameter, respectively.

According to Equations (4)–(9), the thread deformation can be defined by

$$\begin{cases} \delta_{MTi} = \delta_{MT1} + \delta_{MT2} + \delta_{MT3} + \delta_{MT4} + \delta_{MT5e}, \ (M = S \text{ or } R) \\ \delta_{NTi} = \delta_{NT1} + \delta_{NT2} + \delta_{NT3} + \delta_{NT4} + \delta_{NT5e} \end{cases} \quad (10)$$

The corresponding thread stiffness can be written as

$$\begin{cases} K_{MTi} = \dfrac{F_{ri}^{SR}\cos\beta\cos\lambda}{\delta_{MT1} + \delta_{MT2} + \delta_{MT3} + \delta_{MT4} + \delta_{MT5e}}, \ (M = S \text{ or } R) \\ K_{NTi} = \dfrac{F_{ri}^{NR}\cos\beta\cos\lambda}{\delta_{NT1} + \delta_{NT2} + \delta_{NT3} + \delta_{NT4} + \delta_{NT5e}} \end{cases} \quad (11)$$
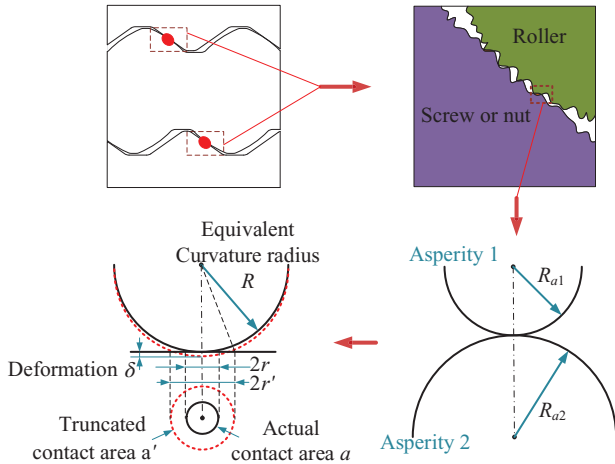
Figure 4. Contact diagram of the contact point of the PRSM.

where, F_{ri}^{SR} and F_{ri}^{NR} are the contact load of the ith thread tooth at the screw–roller and roller–nut interfaces, respectively.

The total thread deformation can be expressed by

$$\delta_T = \delta_{ST} + 2\delta_{RT} + \delta_{NT} \tag{12}$$

2.4. Contact Deformation and Stiffness

The normal contact deformation and stiffness over threads can be calculated by the Hertz contact theory. However, the surface microtopography is not considered by this method. Here, we start from the characterization of rough surface profile and then the microcontact model considering friction factor is built.

2.4.1. Characterization of Rough Surface Profile

Figure 4 illustrates the contact mechanism of the PRSM between the screw or nut thread and roller thread. It can be obviously found that although the contact mode is point contact at screw–roller or nut–roller interfaces, the microcontacts are multiasperity contacts. In order to accurately characterize the contact characteristics of the surface microtopography, the 2D MB function is introduced by[21]

$$z(x) = G^{D-1}(\pi^{1/2}r')^{2-D}\cos\left(\frac{\pi x}{2r'}\right), \left(-r' < x < r', 1 < D < 2\right) \tag{13}$$

where G and D are the fractal roughness and fractal dimension, respectively. r' is the truncated microcontact radius of the asperity and $r' = \sqrt{2}r$.

2.4.2. Microcontact Deformation and Area

The microcontacts between the asperities can be equivalent to rough-on-rigid solution in accordance with Johnson's assumption.[22] According to Equation (13), the microcontact deformation of the asperity can be expressed by

$$\delta = G^{D-1}(\pi^{1/2}r')^{2-D} \tag{14}$$

The actual microcontact area of the asperity is defined by

$$a = \pi r^2 = \frac{1}{2}\pi r'^2 \tag{15}$$

The relation among the asperity deformation δ, equivalent curvature radius R, and truncated radius r' of the asperity can be described by the Pythagorean theorem, as shown in Figure 4, and the equation can be written as

$$R^2 - \left[r'^2 + (R-\delta)^2\right] = 0 \tag{16}$$

As R is much larger than the δ, Equation (16) can be transformed into

$$R \approx \frac{r'^2}{2\delta} \tag{17}$$

Substituting Equations (14) and (15) into Equation (17), the R can be expressed by

$$R = \frac{a^{D/2}}{\pi 2^{1-D/2}G^{(D-1)}} \tag{18}$$

In this paper, only the elastic deformation and plastic deformation are considered for microcontact deformation of the asperity. When the asperity under the normal load exceeds initial yielding, partial elastic deformations are transformed into plastic deformations. Then the critical value of the microcontact deformation from elastic microcontact to plastic microcontact can be obtained as

$$\delta_c = R(\pi K\psi)^2/4 \tag{19}$$

where K is the hardness coefficient and $K = 0.454 + 0.41\nu$. ψ is equal to σ_s/E_0 and E_0 is the equivalent Young's modulus and can be expressed by

$$\frac{1}{2E_0} = \frac{1-\nu^2}{E^2} \tag{20}$$

where the material elastic modulus and Poisson ratio of the screw, roller, and nut are the same.

Substituting Equation (18) into Equation (19) to obtain the following critical microcontact deformation of the asperity

$$\delta_c = \frac{\pi(K\psi)^2(a/2)^{D/2}}{8G^{(D-1)}} \tag{21}$$

when δ is equal to δ_c, the critical elastic microcontact area corresponding to the critical elastic microcontact deformation can be expressed as

$$a_c = \frac{(\pi K^2\psi^2)^{1/(1-D)}}{2^{(4-D)/(1-D)}G^{-2}} \tag{22}$$

2.4.3. Microcontact Area of the Asperity Considering Friction Factor

When the screw and the roller are meshing, there is relative sliding at the meshing point, which causes friction between the

ADVANCED
SCIENCE NEWS
www.advancedsciencenews.com

ADVANCED
THEORY AND
SIMULATIONS
www.advtheorysimul.com

threaded surfaces, and the friction has a direct effect on the thread surface. Hence, the friction factor needs to be considered for the multiscale microcontact mechanic model. When the meshing thread surface has relative sliding friction, the critical average microcontact pressure can be written as[23]

$$\Delta F_f = 1.1 \kappa_f \sigma_s \tag{23}$$

where κ_f denotes the friction correction coefficient and can be defined as follows[24]

$$\kappa_f = \begin{cases} 1 - 0.228\mu, & (0 \leq \mu \leq 0.3) \\ 0.932 \exp\left[-1.528(\mu - 0.3)\right], & (0.3 < \mu \leq 0.9) \end{cases} \tag{24}$$

where μ is the static friction factor.

According to the Hertz contact theory,[23] the mapping relationship between the microcontact load and microcontact deformation of the asperity can be expressed by

$$\delta_e = \left(\frac{3F_e E R^{1/2}}{4}\right)^{2/3} \tag{25}$$

Substituting Equations (18) and (23) into Equation (25) by $F_e = \Delta F_f$, and the critical microcontact deformation considering friction can be written as

$$\delta_{fc} = \frac{\pi(3.3\kappa_f\psi)^2(2a)^{D/2}}{32G^{(D-1)}} \tag{26}$$

Then the critical microcontact area considering friction can be expressed by

$$a_{fc} = (6.6\pi^{1/2}\kappa_f\psi)^{2/(1-D)} 2^{(D-8)/(1-D)} G^2 \tag{27}$$

In previous investigation of the fractal contacts considering friction,[25–27] the above formulas were usually used. However, the calculation of the actual microcontact area did not take into account the changes caused by the friction factors. According to ref. [28], the actual microcontact area is modified by

$$a'_f = (1 + \alpha\mu^2)^{1/2} a \tag{28}$$

where α denotes the contact coefficient and $\alpha = 3.3$.[29]

2.4.4. Surface Microcontact Coefficient

The contact between the screw and the roller could be straight–straight, straight–convex, and convex–concave.[30] Among these contact modes, the third is the most commonly used in PRSM. The difference of the contact modes results in the variations of the actual microcontact area and microcontact load. In addition, the size distribution function of the asperity that microcontact areas are larger than a can be written as

$$n(a) = \begin{cases} \frac{D}{2}(a_L)^{D/2}(a'_f)^{-(D+2)/2}, & (0 < a < a_L) \\ 0, & (a_L < a < +\infty) \end{cases} \tag{29}$$

where a_L denotes the largest microcontact area.

However, Equation (29) is suitable for the contact between two rough surfaces. For example, the thread profiles are not parabolic, circular, and elliptical. In fact, the contact between the screw and the roller is the contact between flat surface and spherical surface. Hence, the surface microcontact coefficient needs to be introduced in order to modify the size distribution function of the asperity. But the previous studies on the surface microcontact coefficient were based on the contact between two rough curved surfaces. The surface microcontact coefficient is defined as follows

$$\xi = \left[\frac{\left(\frac{4}{\pi E}\frac{R_1 R_2}{R_1 + R_2}\right)^{1/2}}{\pi\left(R_1 + R_2\right)}\right]^{1/R_1 + 1/R_2} \tag{30}$$

where R_1 and R_2 are the curvature radii of two thread surfaces, respectively. For the PRSM, the thread profiles of the screw and nut are straight, which means the curvature radius is infinite. It can be found that Equation (30) is not directly suitable for this situation. According to the experience, the curved thread profiles of the screw and nut are very close to the straight thread profile when the nominal diameter is large and the pitch is small. In this situation, the surface microcontact coefficient at the screw–roller and roller–nut interfaces is approximated as Equation (30). The corresponding curvature radius can be expressed by

$$R_X = r_X / \sin\beta \quad (X = S, R, \text{ or } N) \tag{31}$$

Then, the modified size distribution function of the asperity can be written as

$$n'(a) = \xi\frac{D}{2}(a_L)^{D/2}(a'_f)^{-(D+2)/2} \tag{32}$$

2.4.5. Multiscale Contact Mechanic Model Considering Friction

As described above, the contact regimes include elastic contact and plastic contact. According to the value of the critical microcontact area, the actual contact force at single contact point can be divided into the following two types:

1) When $a_L > a_{fc}$, the total actual contact load at single contact position consists of the elastic load and plastic load. That can be expressed by

$$F_r = \frac{EG^{(D-1)}}{3\pi^{1/2}2^{(D/2-3)}}\int_{a_{fc}}^{a_L} n'(a)a'_f{}^{(3-D)/2}da + K\sigma_s\int_0^{a_{fc}} n'(a)a'_f da \tag{33}$$

**ADVANCED
SCIENCE NEWS**

www.advancedsciencenews.com

**ADVANCED
THEORY AND
SIMULATIONS**

www.advtheorysimul.com

In order to simplify the calculation, dimensionless variables are introduced by

$$\begin{cases} F_r{}^* = \dfrac{F_r}{EA_a}, & G^* = \dfrac{G}{\sqrt{A_a}} \\ A_r{}^* = \dfrac{A_r}{A_a}, & a_c{}^* = \dfrac{a_c}{EA_a} \end{cases} \tag{34}$$

Substituting Equations (28), (32), and (34) into Equation (33), the dimensionless microcontact load can be written as Equation (35) when the fractal dimension D is not equal to 1.5

$$F_r{}^* = \xi^{(2-D)/2} \left\{ g_1(D)g_2(D)A_r^{*D/2} \left[\left(\dfrac{(2-D)A_r^*}{\xi D} \right)^{(3-2D)/2} - a_c^{*(3-2D)/2} \right] \right.$$
$$\left. + K\psi(1+\alpha\mu)^{1/2} g_3(D)A_r^{*D/2} a_c^{*(2-D)/2} \right\} \tag{35}$$

where $\quad g_1(D) = \dfrac{[(1+\alpha\mu^2)/\pi]^{1/2}}{G^{*(1-D)}2^{(D-6)/2}}, \quad g_2(D) = \dfrac{D}{3-2D}\left(\dfrac{2-D}{D}\right)^{D/2},$
$g_3(D) = \left(\dfrac{2-D}{D}\right)^{(D-2)}$.
When $D = 1.5$

$$F_r{}^* = \dfrac{(3\xi)^{1/4} G^{(3-2D)/2} g_1(D)}{4} A_r^{*3/4} \ln\left(\dfrac{A_r^*}{3\xi a_c^*} \right)$$
$$+ K\psi(1+\alpha\mu^2)^{1/2}(3a_c^*)^{1/4} A_r^{*3/4} \tag{36}$$

1) when $a_L < a_{fc}$, the total actual contact load at single contact position is plastic load. That can be written by

$$F_r{}^* = K\psi(1+\alpha\mu^2)^{1/2} A_r^* \tag{37}$$

2.4.6. Normal Contact Stiffness

The normal contact stiffness of the single pair of the microcontact asperities is defined as follows

$$k_n = \dfrac{\partial F_{r1}(a)}{\partial \delta} = 2E(a/\pi)^{1/2} \tag{38}$$

where F_{r1} is the microcontact force of the asperity.

However, the microcontact stiffness equation is based on the ideal Hertzian contact model, which is not consistent with the above fractal model. Taking advantage of the 2D MB function to represent the top profile of the asperity, the normal microcontact deformation can be expressed as

$$\delta = G^{(D-1)} a_f'^{(2-D)/2} \tag{39}$$

The relation between normal microcontact deformation and microcontact load of the asperity can be written by

$$F_{r1} = 4ER^{1/2}\delta^{3/2}/3 \tag{40}$$

According to Equations (38)–(40), the normal microcontact stiffness of the asperity considering friction can be expressed as

$$k_n = 4E(a_\mu'/\pi)^{1/2}/3 \tag{41}$$

Hence, the normal contact stiffness of single contact point can be defined by

$$K_n = \int_{a_{fc}}^{a_L} k_n n'(a)\mathrm{d}a = \dfrac{4\xi ED\left[(1+\alpha\mu^2)/\pi\right]}{3(1-D)}$$
$$\times a_L^{D/2}\left[a_L^{(1-D)/2} - a_{fc}^{(1-D)/2} \right] \tag{42}$$

The corresponding dimensionless equation can be expressed by

$$K_n'^* = \dfrac{4\xi(2-D)^{D/2}D^{(2-D)/2}\left[(1+\alpha\mu^2)/\pi\right]}{3(1-D)}$$
$$\times A_r'^{*D/2}\left[\left(\dfrac{2-D}{D}\right)A_r'^{*(1-D)/2} - a_{fc}'^{*(1-D)/2} \right] \tag{43}$$

where $K'_n *$ is the dimensionless normal contact stiffness and $K'_n *= K'/(E\sqrt{A_a})$. A_r' is the actual contact area and can be written by

$$A_r' = \int_0^{a_L} n'(a)a\mathrm{d}a = \dfrac{\xi D}{2-D}a_L \tag{44}$$

2.4.7. Contact Deformation

According to the above analysis, the normal contact deformation of single contact point can be defined by

$$\delta_n = \dfrac{F_r}{K_n} \tag{45}$$

The corresponding axial contact deformation can be written as

$$\delta_C = \dfrac{F_r \cos\beta \sin\lambda}{K_n \cos\beta \sin\lambda} \tag{46}$$

2.4.8. Load Distribution Model

The load distribution is an important content for the PRSM and associated with the investigation of contact stress, transmission efficiency, energy loss, thermal conductivity, and fatigue life. Hence, it is essential to calculate the contact force at each thread tooth.

Figure 5 shows the sketch of the static load of the PRSM under "T-C" load condition. It can be seen that the deformations include thread deformation, compression deformation of shaft section, and contact deformation.[3] The load distribution model at the screw–roller interface can be defined by

$$\dfrac{F_{ri}^{SR}-F_{ri+1}^{SR}}{K_{SRC}} - \left[\dfrac{F_{a1}/(\sin\beta\cos\lambda)-\sum_{j=1}^{i}F_{rj}^{SR}}{K_{SS}} \right.$$
$$\left. + \dfrac{F_{ri+1}^{SR}-F_{ri}^{SR}}{K_{ST}} - \dfrac{\sum_{j=1}^{i}(F_{rj}^{SR}-F_{rj}^{NR})}{K_{RS}} - \dfrac{F_{ri+1}^{SR}-F_{ri}^{SR}}{K_{RT}} \right] \sin\beta\cos\lambda = 0 \tag{47}$$

where F_{ri}^{SR} and F_{ri}^{NR} are the contact load of the ith thread tooth at the screw–roller and roller–nut interfaces, respectively. They correspond to the contact force in Equation (33). K_{SRC} is the contact

ADVANCED
SCIENCE NEWS
www.advancedsciencenews.com

ADVANCED
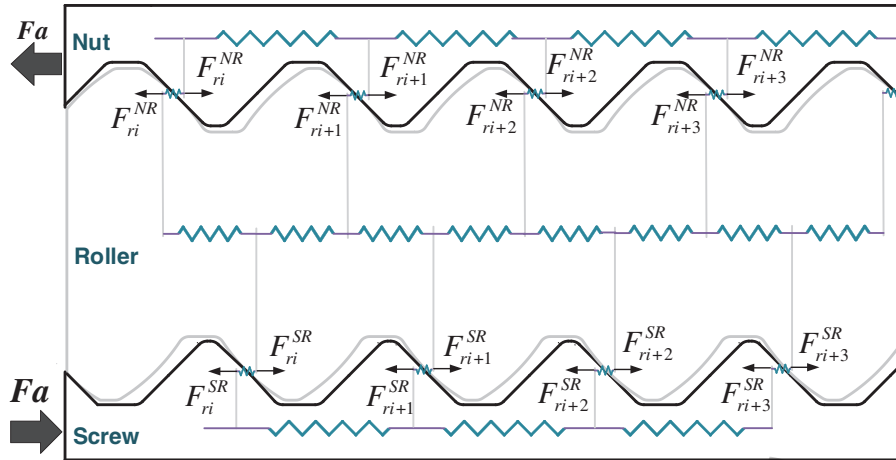THEORY AND
SIMULATIONS
www.advtheorysimul.com

Figure 5. Sketch of the load distribution of the PRSM.

stiffness at the screw–roller interface and corresponds to the normal contact stiffness in Equation (42). F_{a1} is the total axial load of single roller and $F_{a1} = F/n$. K_{ST} and K_{RT} are the thread stiffness of the screw and the roller, respectively. K_{SS} and K_{RS} are the shaft section of the screw and the roller, respectively. K_{SS} and K_{RS} can be expressed by[3]

$$\begin{cases} K_{SS} = \frac{\pi E r_S^2}{np} \\ K_{RS} = \frac{\pi E r_R^2}{2p} \end{cases} \tag{48}$$

The dimensionless equation of the load distribution at the screw–roller interface can be expressed by

$$\frac{F_{ri}^{SR*} - F_{ri+1}^{SR*}}{K_{SRC}^*} - \left[\frac{F_{a1}^*/(\sin\beta\cos\lambda) - \sum_{j=1}^{i} F_{rj}^{SR*}}{K_{SS}^*} \right.$$
$$+ \frac{F_{ri+1}^{SR*} - F_{ri}^{SR*}}{K_{ST}^*} - \frac{\sum_{j=1}^{i}(F_{rj}^{SR*} - F_{rj}^{NR*})}{K_{RS}^*} - \left. \frac{F_{ri+1}^{SR*} - F_{ri}^{SR*}}{K_{RT}^*} \right] \sin\beta\cos\lambda = 0 \tag{49}$$

where these dimensionless variables are introduced by

$$\begin{cases} K_{SRC}^* = \frac{K_{SRC}}{E\sqrt{A_a}}, \ K_{SS}^* = \frac{K_{SS}}{E\sqrt{A_a}}, \ K_{RS}^* = \frac{K_{RS}}{E\sqrt{A_a}} \\ K_{ST}^* = \frac{K_{ST}}{E\sqrt{A_a}}, \quad K_{RT}^* = \frac{K_{RT}}{E\sqrt{A_a}}, \ F_r^* = \frac{F_r}{EA_a} \end{cases} \tag{50}$$

where A_a is the nominal microcontact area and can be identified through the power spectrum.[31]

Similarly, the dimensionless equation of the load distribution at the roller–nut interface can be written by:

$$\frac{F_{ri}^{NR*} - F_{ri+1}^{NR*}}{K_{NRC}^*} + \left[\frac{F_{a1}^*/(\sin\beta\cos\lambda) - \sum_{j=1}^{i} F_{rj}^{NR*}}{K_{NS}^*} \right.$$
$$+ \frac{F_{ri+1}^{NR*} - F_{ri}^{NR*}}{K_{NT}^*} - \frac{\sum_{j=1}^{i}(F_{rj}^{SR*} - F_{rj}^{NR*})}{K_{RS}^*} + \left. \frac{F_{ri+1}^{NR*} - F_{ri}^{NR*}}{K_{RT}^*} \right] \sin\beta\cos\lambda = 0 \tag{51}$$

$$\begin{cases} K_{NRC}^* = \frac{K_{NRC}}{E\sqrt{A_a}}, \quad K_{NS}^* = \frac{K_{NS}}{E\sqrt{A_a}} \\ K_{NT}^* = \frac{K_{NT}}{E\sqrt{A_a}} \end{cases} \tag{52}$$

According to Equations (35), (49), and (51), the dimensionless equation of the load distribution is a function of A_r. Hence, the actual contact areas and contact forces over threads can be obtained by these equations.

3. Modeling Algorithms

The overall calculation processing of the axis stiffness and load distribution is shown in **Figure 6**, and systematically explained as follows:

1) Input the machining parameters, design parameters, and working parameters.
2) Compute the critical microcontact area with friction factor by Equation (24). Compute the fractal surface microcontact coefficient by Equation (30).
3) Given the maximum initial microcontact area a_L. Compute the actual contact load F_{ri} and normal contact stiffness K_n by Equation (33) and Equation (42) at the corresponding maximum microcontact area, respectively.
4) Compute the thread stiffness K_T and shaft section stiffness K_S by Equation (11) and Equation (48), respectively.
5) Compute the distribution of the actual contact area A_r and contact force F_{ri} by Equations (35), (49), and (51).
6) Compute the total axial contact load $F_{a0} = nF_{a1} = n\sum_{i=1}^{n_t} F_{ri}$. If $\tau = |F_{a0} - F_a|/F_{a0} > \varepsilon$, then $a_L = a_L \pm \Delta a_L$. Jump to step (4) and recalculate the contact stiffness and contact load until $|F_a - F_{a0}|/F_a < \varepsilon$.
7) Compute the normal contact deformation, thread deformation, and screw shaft deformation by Equations (46), (3), and (12). Compute the axial stiffness by Equation (1).
8) Output the load distribution and axial stiffness.

4. Numerical Examples and Discussion

In this section, an investigation on the static contact load and axial stiffness of the PRSM is carried out by numerical calculations. These results cover the load distribution and axial stiffness by considering the effects of the nut position, fractal roughness,
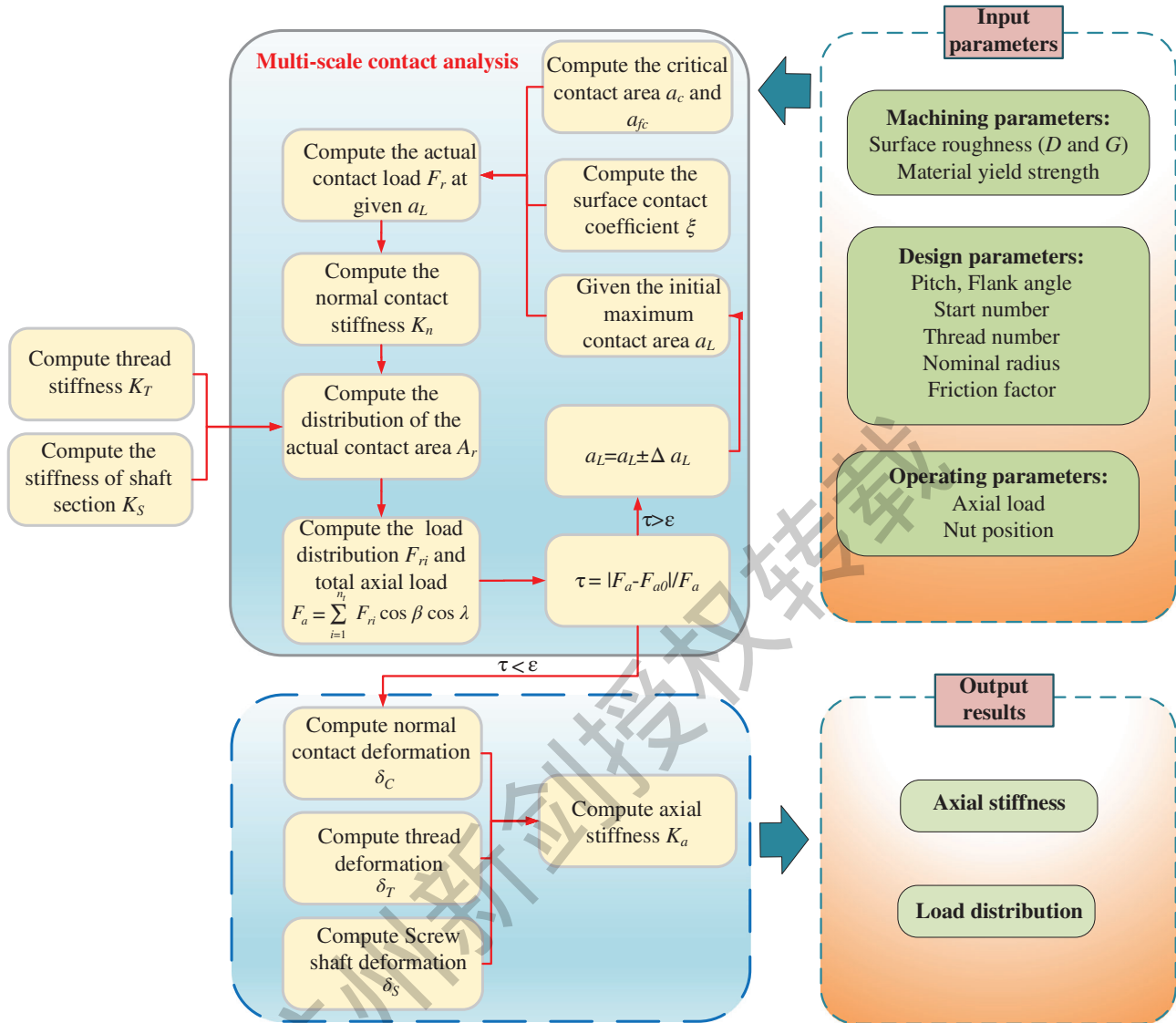
Figure 6. Flowchart of the calculation of the load distribution and axial stiffness.

fractal dimension, material yield strength, friction factor, and axial load. The major design parameters in each example are described in **Table 1**. Moreover, the thickness of the thread root is 1.95 mm, the thread thickness is 0.85 mm, and the root height is 0.55 mm. The transmission efficiency of the PRSM is 85%. The material elastic modulus and shear modulus are 750 MPa and 79 GPa.

4.1. Model Verification and Comparison

4.1.1. Load distribution

To further verify the credibility of the load distribution model in current work, a comparison with ref. [3] is conducted under the same conditions. **Figure 7** shows the load distribution at the screw–roller and roller–nut interfaces, when the axial load is

Table 1. Design parameters of the PRSM.

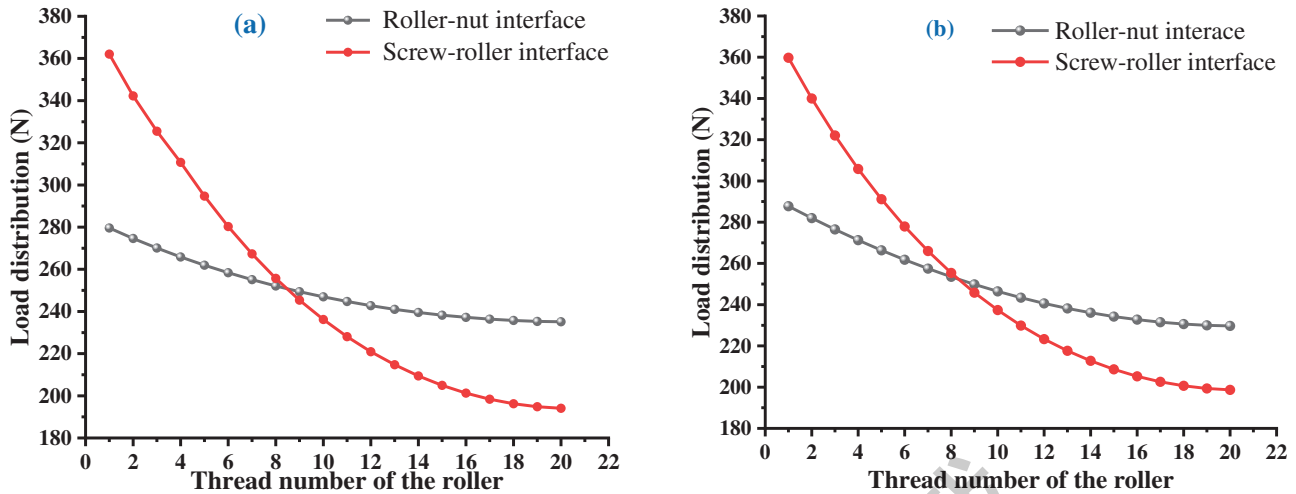| Parameters	Screw	Roller	Nut
Radius (mm)	12	4	20
Flank angle (rad)	$\pi/4$	$\pi/4$	$\pi/4$
Helix angle (rad)	0.1319	0.0794	0.0794
Pitch (mm)	2	2	2
Start	5	1	5
External radius (mm)	/	/	27.5
Roller number	/	10	/
Thread number	/	20	/

Figure 7. Load distribution over threads of the PRSM in different methods. a) Contact forces of the roller threads in ref. [3]; b) contact forces of the roller threads in current work.
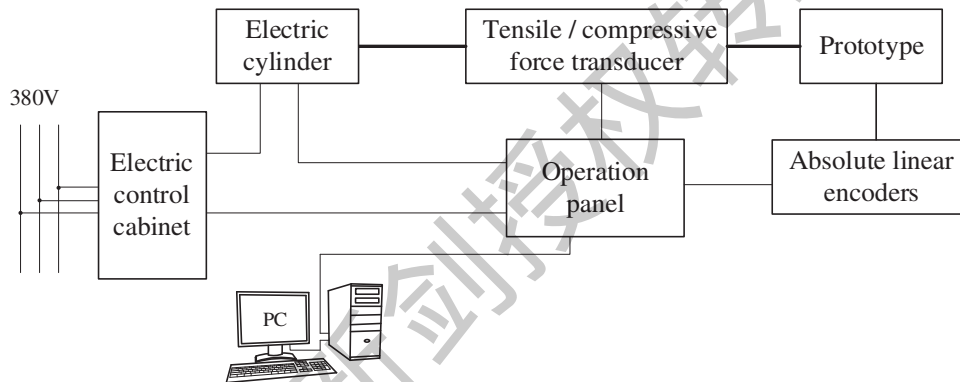

Figure 8. Layout of the axial stiffness test-bed.

50 kN and the surface roughness is Ra 0.3 ($G = 2.9321 \times 10^{-6}$ mm and $D = 1.6073$), and the friction factor at the screw–roller and roller–nut interfaces are 0.05 and 0.03, respectively. It is obviously found from Figure 7 that the contact forces at the screw–roller interface are almost the same, while those at the roller–nut interface are slightly different. The maximum contact force in current work increases by 1.79% and the minimum contact force decreases by 2.1% compared to the results of the roller–nut interface in ref. [3]. It can be also found from Figure 7 that although the approaches are different, the results are very anastomotic between the current work and ref. [3]. To this end, based on the aforementioned analysis, it can be validated that the results of the load distribution conducted in current article are credible.

4.1.2. Axial stiffness

Axial stiffness is a vital performance indicator of the PRSM, and it plays an important role on the transmission accuracy and dynamic characteristic of the PRSM. Therefore, it is necessary to estimate the axial stiffness in accordance with the working position and external load. In order to further confirm the correct-ness of the calculation results of axial stiffness, the results of experiment and finite element method (FEM) are used to compare under the same working conditions. The test-bed layout of the axial stiffness is shown in **Figure 8**, and the test site is shown in **Figure 9**. During the test of the axial stiffness, the input end of the screw of the tested PRSM is locked with an expansion sleeve, and then the value of the axial force is manually increased on the operation panel, and the actual axial force and the corresponding axial deformation are both recorded. The electric cylinder (Park ETH100M10C1P1CBMN0400A) is used to apply the axial force to the PRSM. The applied force of the PRSM measured by the tensile/compressive force transducer (HBM U3) is ΔF_a, and the output axial deformation of the PRSM measured by the grating ruler (Heidenhain LC 485) is $\Delta \delta_a$, then the axial stiffness of the PRSM is $K_a = \Delta F_a / \Delta \delta_a$.

Figure 10 shows the effects of the axial load and nut position on the axial stiffness through theory, simulation, and experiment. The axial loads change from 20 to 45 kN and the nut position varies from 60 to 120 mm. As shown in Figure 10, it can be clearly found that the predicted results by theoretical calculation are relatively consistent with the FEM and test results. As can be seen from Figure 10a–c that the maximum relative error of the axial
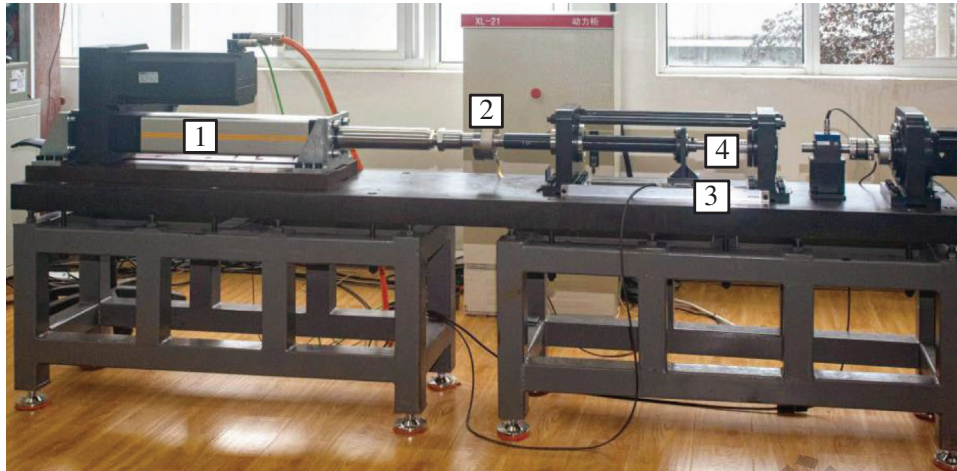
**ADVANCED
SCIENCE NEWS**
www.advancedsciencenews.com

**ADVANCED
THEORY AND
SIMULATIONS**
www.advtheorysimul.com

Figure 9. Testing site. 1) Electric cylinder, 2) tensile/compressive force transducer, 3) grating ruler, 4) prototype.
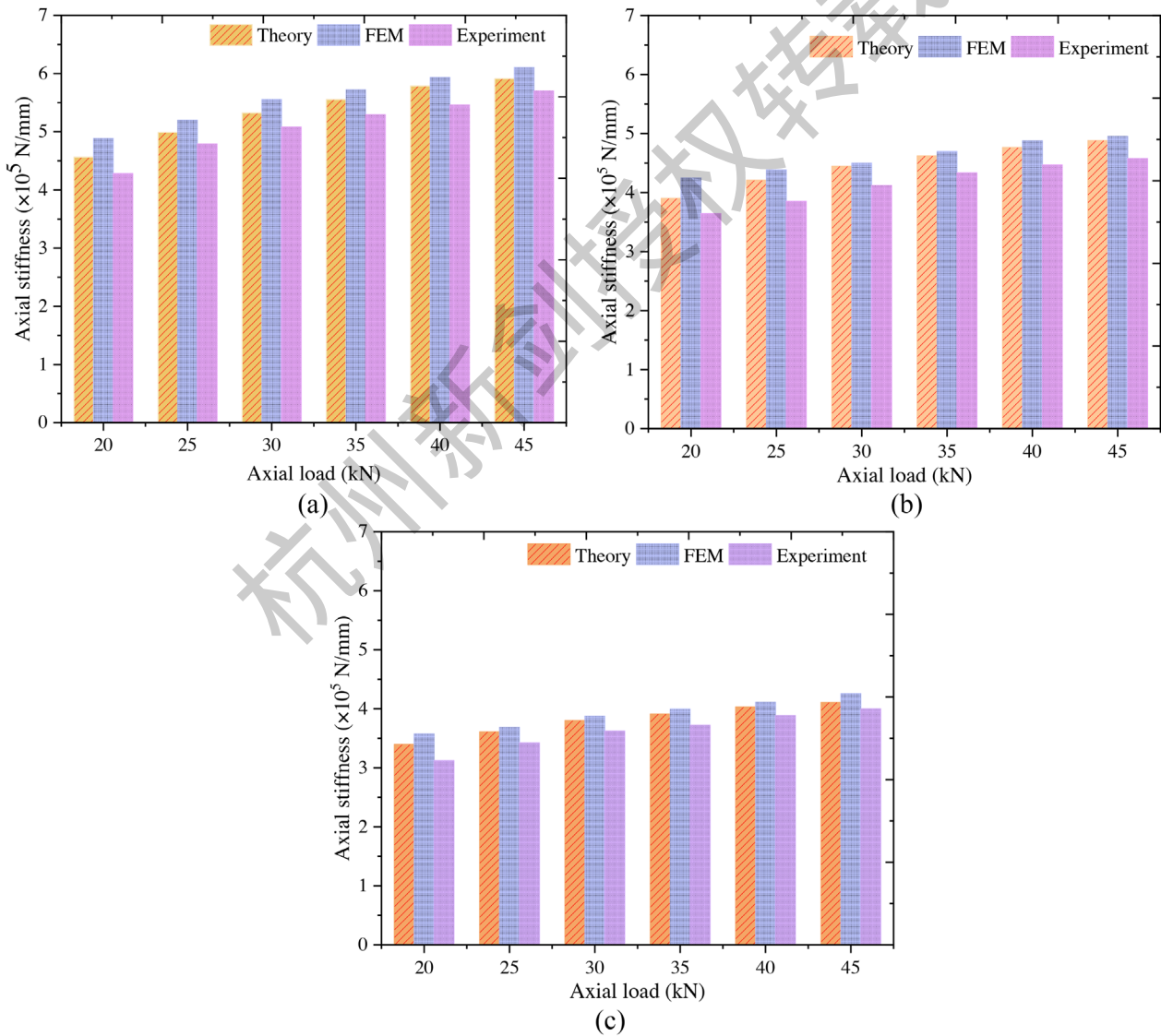

(a)

(b)

(c)

Figure 10. The variations of the axial stiffness versus the axial load and nut position: a) the nut position $L_N = 60$ mm; b) the nut position $L_N = 90$ mm; c) the nut position $L_N = 120$ mm.
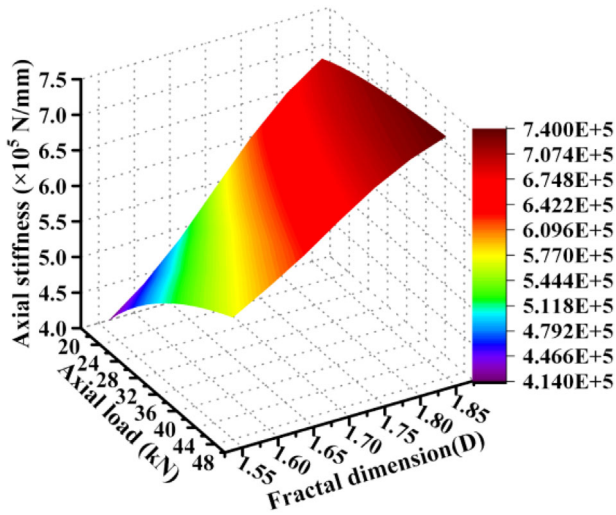
**ADVANCED
SCIENCE NEWS**
www.advancedsciencenews.com

**ADVANCED
THEORY AND
SIMULATIONS**
www.advtheorysimul.com

Figure 11. Axial stiffness under different axial load and fractal dimension.

stiffness between the results obtained by the theoretical calculation and by FEM is 8.3%, and that between the results obtained by the theoretical calculation and by the test is 11.9%. During the test, the axial deformation data collected by the grating ruler include the structural deformation of the test bench, so that the axial stiffness of the test is smaller.

Figure 10 presents variations of the axial stiffness versus the axial load and nut position. It can be seen that under the same nut position, the larger the axial load, the higher the axial stiffness. In addition, it can be found that under the same axial load, the axial stiffness reduces as the nut position increasing. The main reason is that the increase of the nut position results in the increase of the screw shaft deformation, which is obtained by Equation (3).

4.2. Effect of the Fractal Parameters

The thread surface quality is directly related to fractal parameters. These parameters mainly consider fractal dimension and fractal roughness.

4.2.1. Effect of the Fractal Dimension

In **Figure 11**, the axial stiffness is calculated under the different axial load and fractal dimension. The detailed parameters are shown below: the axial loads change from 20 to 50 kN, the fractal roughness is $G = 2.9321 \times 10^{-9}$ m, the friction factors at the screw–roller and roller–nut interfaces are 0.05 and 0.03, the yield strength is 750 MPa. It can be obviously found that with the fractal dimension increasing, the axial stiffness monotonically increases. The main reason for the phenomenon is that the bigger the fractal dimension, the more the high frequency components, the smoother the thread surface. That is consistent with ref. [32]. In addition, the axial stiffness rises as the growth of the axial load. When the fractal dimension is small, the axial stiffness changes more obviously with the axial force. When the fractal dimension is large, the axial stiffness varies slightly with the axial force. Therefore, it can be concluded that the large fractal dimension is beneficial to achieve high and stable axial stiffness.

In **Figure 12**, the contact forces are computed under the different axial load and fractal dimension. We can find from Figure 12a that under the same fractal dimension, the contact force at the screw–roller interface decreases as the thread number increasing. Moreover, the larger the fractal dimension, the more uneven the load distribution. In the first few threads of the roller, the contact force increases with the fractal dimension increasing; while in the last few threads, the contact force decreases with the growth of the fractal dimension. The variation trend of the load distribution at the roller–nut interface is similar with that at the screw–roller interface.

4.2.2. Effect of the Fractal Roughness

Figure 13 shows the variation of the axial stiffness under the different fractal roughness and axial load. The engineering parameters are the same as the above. It can be found from Figure 13 that with the fractal roughness increasing, the axial stiffness monotonically decreases. The main reason for the phenomenon is that the larger the fractal roughness, the higher the amplitude of the
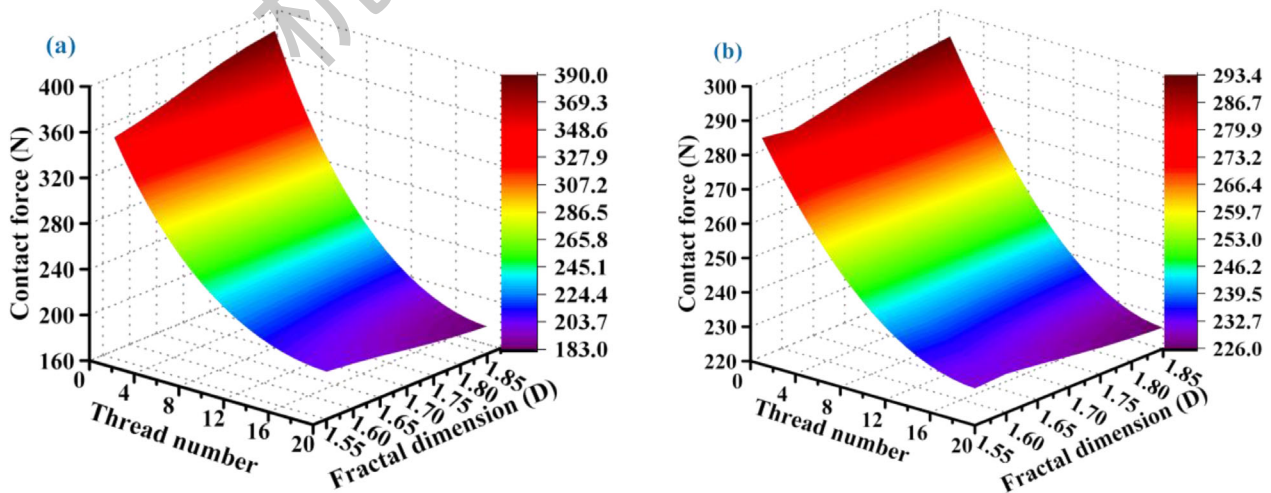

Figure 12. Load distribution under the different thread number and fractal dimension. a) The variation of the load distribution of the screw–roller interface. b) The variation of load distribution of the roller–nut interface.
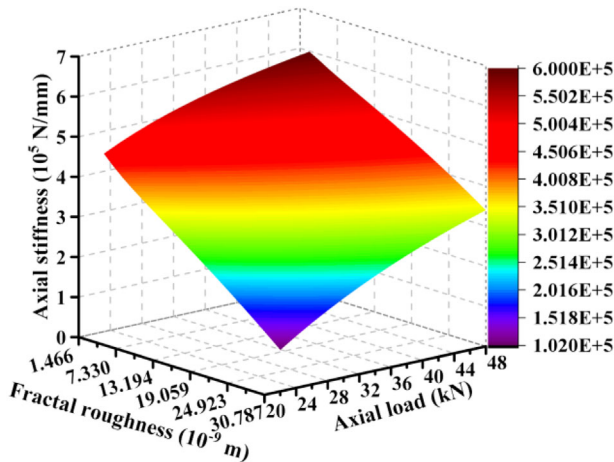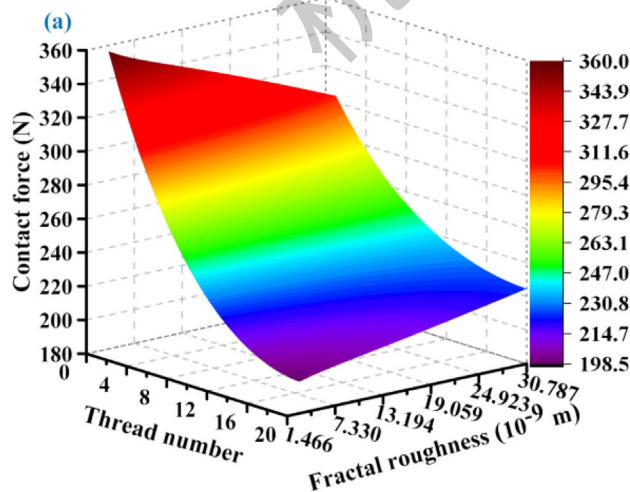
ADVANCED
SCIENCE NEWS
www.advancedsciencenews.com

ADVANCED
THEORY AND
SIMULATIONS
www.advtheorysimul.com

Figure 13. Axial stiffness under the different axial load and fractal roughness.

4.3. Effect of the Friction Factor

In **Figure 15**, the axial stiffness is computed under the different friction factors and axial loads. It can be found from Figure 15a,b that under the same axial load, the axial stiffness reduces slightly when the friction factor changes from 0.01 to 0.2; while the axial stiffness notably decreases when the friction factor varies from 0.31 to 0.5. The difference between different intervals can be explained by Equation (24). However, the friction factor is less than 0.3 in engineering application.[33,34] Moreover, under the same friction factor, the axial stiffness rises significantly with the growth of the axial load.

Figure 16 shows the load distribution against the friction factor and thread number. It can be found that the load distribution is almost unchanged when the friction factor varies from 0.01 to 0.2. As mentioned before, the load distribution also mainly considers the situation where the friction factor is less than 0.3. Hence, the load distribution is almost unchanged when the friction factor is small.

surface topography, and the rougher the thread surface. As a result, the axial stiffness is smaller. Therefore, it can be concluded that the smaller fractal roughness is beneficial to improve the axial stiffness.

Figure 14 indicates the dependence of the load distribution on the thread number and fractal roughness. It can be obviously seen from Figure 14a that the uniformity of the contact force at the screw–roller interface increases significantly as the fractal roughness increases. In other words, the contact forces decrease with the increase of the fractal roughness in the first few threads, while those increase slightly in the rest threads. The reason is that the surface is rougher as the growth of the fractal roughness, but the actual contact area decreases. That leads to the variation of the load distribution. In addition, the variation trend of the load distribution at the roller–nut interface is consistent with that at the screw–roller interface. Hence, it can be concluded that the larger fractal roughness has an advantage of improving the uniformity of the load distribution.

4.4. Effect of the Material Properties

The axial stiffness is calculated under the different material yield strength and axial load, as shown in **Figure 17**. The axial stiffness increases significantly according to a yield strength increment, while the increment rate of the axial stiffness reduces with material yield strength increasing. The difference of the material yield strength could be derived from the heat treatment methods or processing methods such as fine grinding or rolling. For the bearing steel, the material yield strength is generally 750 MPa, and the corresponding axial stiffness is about 5.7872×10^5 N mm^{-1}. In addition, it can be found from Figure 17 that, under the same material yield strength, the axial stiffness increases when the axial load changes from 20 to 35 kN. Thus, it can be concluded that the material yield strength and axial load have a great influence on the axial stiffness of the PRSM.

Figure 18 illustrates the load distribution against the material yield strength and thread number. As shown in Figure 18a, it can
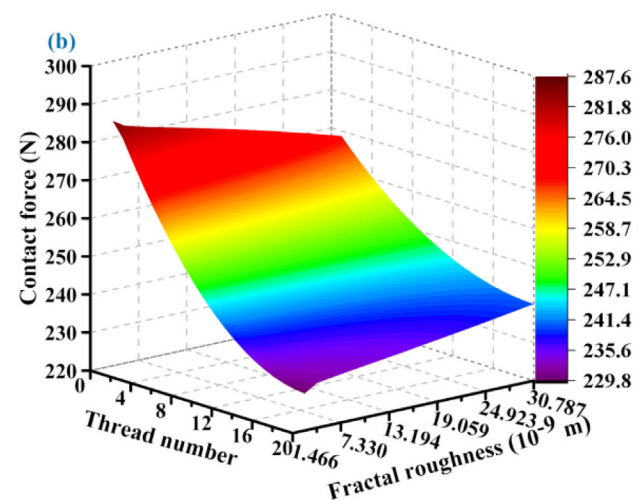

Figure 14. Load distribution under the different thread number and fractal roughness ($D = 1.6073$). a) The variation of load distribution of the screw–roller interface. b) The variation of load distribution of the roller–nut interface.
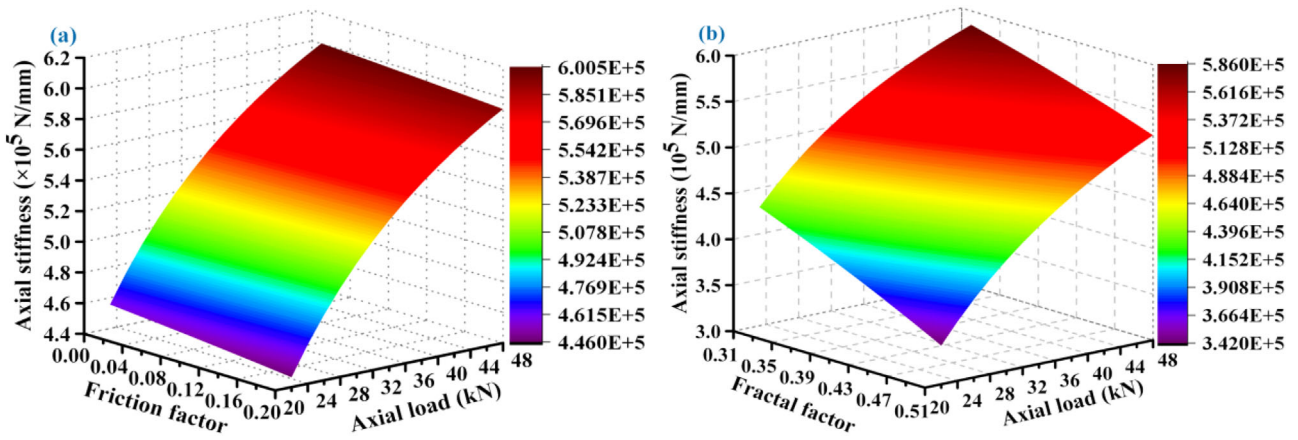
**ADVANCED
SCIENCE NEWS**

www.advancedsciencenews.com

**ADVANCED
THEORY AND
SIMULATIONS**

www.advtheorysimul.com

Figure 15. Axial stiffness under different axial load and friction factor. a) The friction factor changes from 0.01 to 0.2. b) The friction factor varies from 0.31 to 0.5.
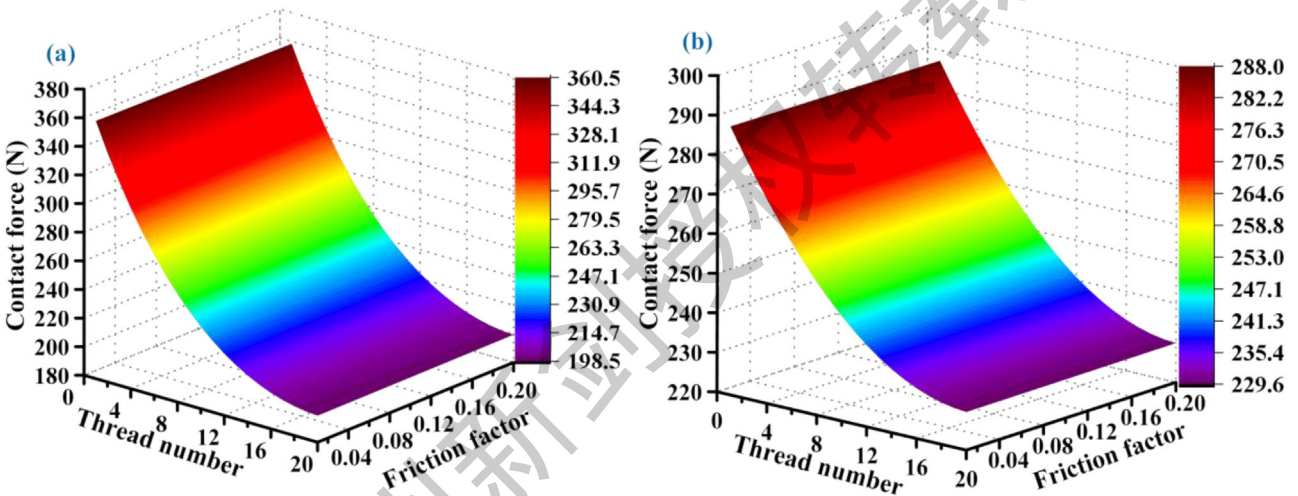

Figure 16. Load distribution under the different thread number and friction factor. a) The variation of contact forces of the screw–roller interface. b) The variation of contact forces of the roller–nut interface.
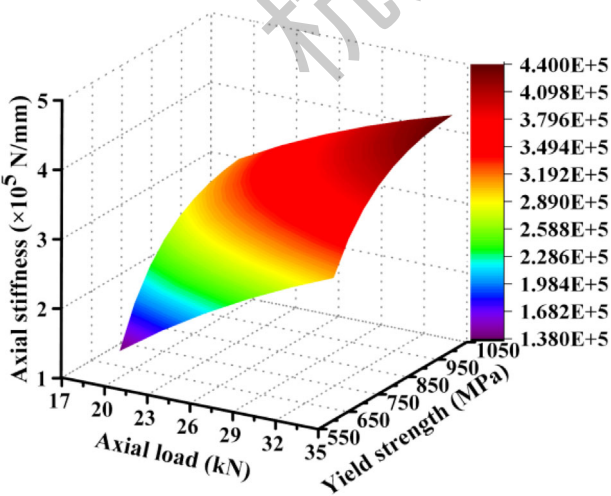

Figure 17. Axial stiffness under the different axial load and material yield strength.

be seen that at the screw–roller interface, the contact force increases but the increment rate decreases with the increase of material yield strength when the thread number of the roller is the first 9 teeth. However, the contact force decreases with the growth of material yield strength when the thread number of the roller is the remaining. Moreover, Figure 18b shows that the variation of the contact force at the roller–nut interface is consistent with that at the screw–roller interface. Thus, we can find that the material yield strength plays an important role on the load distribution of the PRSM.

5. Conclusions

In this paper, the axial stiffness and load distribution models suitable for the PRSM are presented by considering the surface microtopography and friction factor. The rough surface topography is characterized by the 2D fractal function. The multiscale microcontact model is built by considering elastic and plastic contact regimes to calculate the total actual contact area used
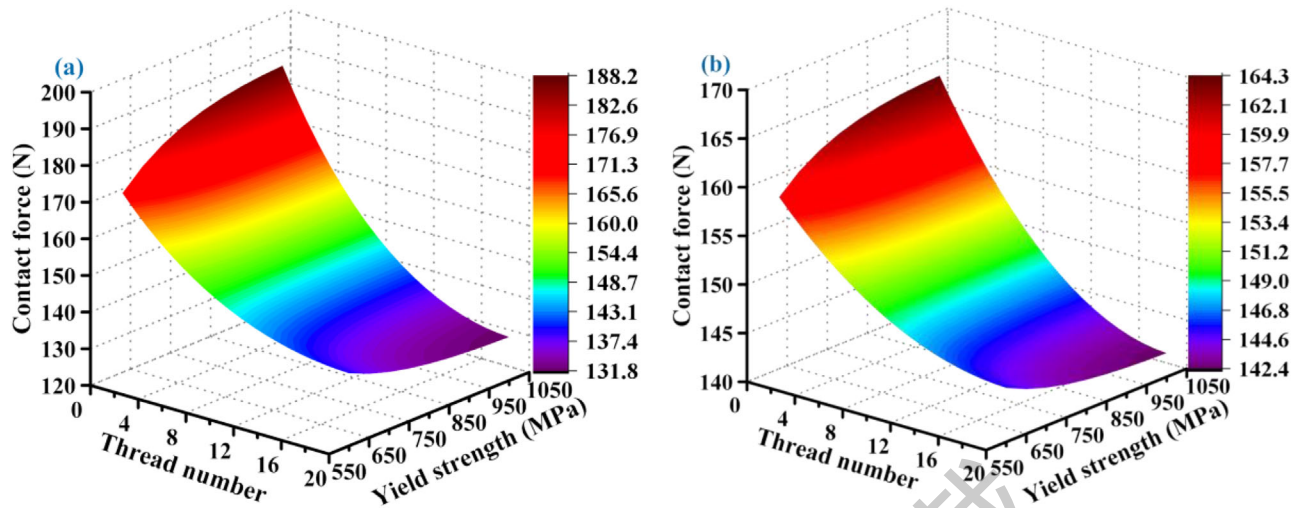
Figure 18. Load distribution under the different thread number and yield strength. a) The variation of contact force of the screw–roller side. b) The variation of contact force of the roller–nut side.

in the load distribution. The multiscale microcontact model is modified by introducing the surface microcontact coefficient in order to accurately characterize the microcontact characteristics of the thread profile. Then, the influences of the nut position, fractal dimension, fractal roughness, friction factor, axial load, and material yield strength on the axial stiffness and load distribution are furtherly studied. The main contributions and conclusions are summarized as follows:

1) The effect of the nut position of the PRSM on the axial stiffness is large. The axial stiffness decreases with the increase of the nut position when the axial load is fixed. In addition, when the nut position is fixed, the larger the axial load, the greater the axial stiffness.

2) The fractal dimension has a great influence on the axial stiffness. The larger the fractal dimension, the smoother the thread surface, and the higher the axial stiffness. It is effective to improve the axial stiffness by improving thread surface quality. Whereas, the load distribution is slightly influenced by the fractal dimension when the dimension varies from 1.55 to 1.85.

3) The influence of the fractal roughness on the variation of the axial stiffness and load distribution is obvious. The axial stiffness monotonically decreases with the fractal roughness increasing. The larger the fractal roughness, the higher the amplitude of the surface topography, and the rougher the thread surface. As a result, the axial stiffness is smaller, while the uniformity of the load distribution is better. Hence, the axial stiffness and load distribution should be comprehensively considered when the fractal roughness is selected.

4) The axial stiffness reduces slightly with the growth of the friction factor when the factor is less than 0.3, while that decreases significantly when the factor is more than 0.3. Moreover, the variation rule of the load distribution is consistent with the axial stiffness.

5) The increase of the material yield strength is beneficial to improve the axial stiffness when the friction factor and fractal parameters are fixed. But the unevenness of load distribution increases as adding of material yield strength. Therefore, the selection of the material yield strength should consider the axial stiffness and load distribution at the same time.

Conflict of Interest

The authors declare no conflict of interest.

Data Availability Statement

The data that support the findings of this study are available from the corresponding author upon reasonable request.

[1] J.-C. MarÉ, J. Fu, *Chin. J. Aeronaut.* **2017**, *30*, 857.

[2] G. Qiao, G. Liu, Z. Shi, Y. Wang, S. Ma, T. C. Lim, *Proc. Inst. Mech. Eng., Part C* **2018**, *232*, 4128.

[3] W. Zhang, G. Liu, R. Tong, S. Ma, *Proc. Inst. Mech. Eng., Part C* **2016**, *230*, 3304.

[4] W. Zhang, G. Liu, S. Ma, R. Tong, *Proc. Inst. Mech. Eng., Part C* **2019**, *233*, 4653.

[5] X. Du, B. Chen, Z. Zheng, *Tribol. Int.* **2021**, *154*, 106689.

[6] M. H. Jones, S. A. Velinsky, *Mech. Based Des. Struct. Mach.* **2014**, *42*, 17.

[7] F. Abevi, A. Daidie, M. Chaussumier, S. Orieux, *J. Mech. Rob.* **2016**, *8*, 041020.

[8] F. Abevi, A. Daidie, M. Chaussumier, M. Sartor, *J. Mech. Des.* **2016**, *138*, 012301.

[9] S. Ma, G. Wu, J. Zhang, G. Liu, *MATEC Web Conf.* **2020**, *306*, 05001.

[10] D. Guan, L. Jing, J. Gong, H. Shen, H. H. Hilton, *Tribol. Int.* **2018**, *124*, 117.

[11] R. Wang, L. Zhu, C. Zhu, *Int. J. Mech. Sci.* **2017**, *134*, 357.

[12] Z. Zhao, H. Han, P. Wang, H. Ma, S. Zhang, Y. Yang, *Mech. Mach. Theory* **2021**, *158*, 104219.

[13] Z. Q. Gong, K. Komvopoulos, *J. Tribol.* **2005**, *127*, 331.

[14] X. Yin, K. Komvopoulos, *Int. J. Solids Struct.* **2010**, *47*, 912.

[15] E. Milanese, T. Brink, R. Aghababaei, J.-F. Molinari, *Nat. Commun.* **2019**, *10*, 1116.

[16] Y. Chang, J. Ding, Z. He, A. Shehzad, Y. Ding, H. Lu, H. Zhuang, P. Chen, Y. Zhang, X. Zhang, Y. Chen, *Int. J. Mach. Tools Manuf.* **2020**, *158*, 103609.

[17] J. H. Han, P. Shan, S. S. Hu, *Mater. Sci. Eng., A* **2006**, *435–436*, 204.

[18] C. Ma, J. Yang, L. Zhao, X. Mei, H. Shi, *Appl. Therm. Eng.* **2015**, *86*, 251.

[19] S. Ma, W. Cai, L. Wu, G. Liu, C. Peng, *Mech. Mach. Theory* **2019**, *134*, 151.

[20] S. Yamamoto, *Theory and Calculation of Screw Thread Connection*, Shanghai Science and Technology Literature Press, Shanghai **1984**.

[21] A. Majumdar, B. Bhushan, *J. Tribol.* **1990**, *112*, 205.

[22] K. L. Johnson, J. A. Greenwood, J. G. Higginson, *Int. J. Mech. Sci.* **1985**, *27*, 383.

[23] K. L. Johnson, *Contact Mechanics*, Cambridge University Press, New York **1985**.

[24] W. Pan, X. Li, L. Wang, N. Guo, J. Mu, *Eur. J. Mech., A* **2017**, *66*, 94.

[25] X. Li, B. Yue, G. Zhao, D. Sun, *Adv. Mech. Eng.* **2014**, *2014*, 378518.

[26] X. Li, G. Zhao, Y. Liang, X. Ju, *Int. J. Ind. Syst. Eng.* **2014**, *18*, 418.

[27] W. Pan, X. Li, L. Wang, J. Mu, Z. Yang, *Acta Mech.* **2018**, *229*, 2149.

[28] J. S. Courtney-Pratt, E. Eisner, *Proc. R. Soc. London, Ser. A* **1957**, *238*, 529.

[29] J. S. McFarlane, D. Tabor, *Proc. R. Soc. London, Ser. A* **1950**, *202*, 244.

[30] S. Sandu, N. Biboulet, D. Nelias, F. Abevi, *Mech. Mach. Theory* **2018**, *126*, 243.

[31] J. Liu, C. Ma, S. Wang, *Mech. Syst. Signal Process.* **2020**, *135*, 106397.

[32] K. Huang, Y. Xiong, T. Wang, Q. Chen, *Appl. Surf. Sci.* **2017**, *392*, 8.

[33] S. Ma, L. Wu, X. Fu, Y. Li, G. Liu, *Mech. Mach. Theory* **2019**, *139*, 212.

[34] Z. Xie, Q. Xue, J. Wu, L. Gu, L. Wang, B. Song, *Tribol. Int.* **2019**, *140*, 105883.